

AD A098821

DTIC FILE COPY

5

OFFICE OF NAVAL RESEARCH
Contract N00014-79-0622
Task No. NR 056-729
TECHNICAL REPORT NO. 4
Creation and Structure Study of Vacuum
Isolated Clusters of Argon, Krypton and Xenon

by
S. S. Kim and G. D. Stein
Prepared for Publication
in

Journal of Colloid and Interface Science

Northwestern University
Departments of Mechanical and Nuclear Engineering,
Chemistry, and Physics
Evanston, Illinois 60201

April, 1981

Reproduction in whole or in part is permitted for
any purpose of the United States Government

This document has been approved for public release
and sale; its distribution is unlimited

SECURITY CLASSIFICATION OF THIS PAGE (This Page Being)		REPORT DOCUMENTATION PAGE	
1. REPORT NUMBER	2. REPORT ACCESSION NUMBER	3. REPORT NUMBER	4. REPORT NUMBER
Technical Report No. 4	AD-A098821		
5. TYPE OF REPORT & PERIOD COVERED		6. PERFORMING ORG. REPORT NUMBER	
Interim		N00014-79-0622	
7. AUTHOR(s)		8. CONTRACT OR GRANT NUMBER(s)	
S. S. Kim and G. D. Stein		N00014-79-0622	
9. PERFORMING ORGANIZATION NAME AND ADDRESS		10. PROGRAM ELEMENT, PROJECT, TASK AREA & WORK UNIT NUMBERS	
Northwestern University, Departments of Mechanical and Nuclear Engineering, Chemistry, and Physics Evanston, Illinois 60201		MR 056-729	
11. CONTROLLING OFFICE NAME AND ADDRESS		12. REPORT DATE	
Office of Naval Research Chemistry Program Code 472 Arlington, Virginia 22217		APR 1981	
13. MONITORING AGENCY NAME & ADDRESS (if different from 11)		14. SECURITY CLASS. (of this report)	
ONR, Chicago 536 S. Clark Street Chicago, Illinois 60605		Unclassified	
15. DISTRIBUTION STATEMENT (of this Report)		16. SECURITY CLASS. (of this page)	
Distribution of this document has been approved for public release and sale; its distribution is unlimited.		Unclassified	
17. DISTRIBUTION STATEMENT (of this page)		18. SECURITY CLASS. (of this page)	
(15) N00014-79-C-0622		Unclassified	
19. SUPPLEMENTARY NOTES		20. ABSTRACT (Continue on reverse side if necessary; use separate sheet for abstract)	
Prepared for publication in Journal of Colloid and Interface Science		Clusters, Nucleation, Laval nozzles, Electron diffraction, Structure, Ar, Kr, Xe	
21. KEY WORDS (Continue on reverse side if necessary; use separate sheet for keywords)		22. ABSTRACT (Continue on reverse side if necessary; use separate sheet for abstract)	
		Homogeneous clusters of Ar, Kr or Xe are formed in adiabatic, high Mach number expansions through very small, diverging Laval nozzle sources. A He carrier gas is employed and the mole fraction of condensable species varied from 1.0 to 0.06 in an effort to control the cluster size distribution and temperature. The nozzle source is part of a multi-stage molecular beam apparatus. Electron diffraction, using a 40 keV beam, is used to study cluster structure. Cluster sizes are varied from $g = 50$ to 1,500 atoms per cluster and temperatures range from 20 to 60 K. The structure for $g > 1,000$	

DD FORM 1 JAN 73 1473
GPO : 1973-011-60011

SECURITY CLASSIFICATION OF THIS PAGE (This Page Being)

81 5 12 038

245-760

72

Technical Rept.

MAILED
MAY 13 1981

Rang Soo Kim
Gilbert D. Stein

20. is bulk f.c.c. and transforms gradually into a non-crystalline structure as size decreases. The smallest structures, for all three noble gases, are consistent with the icosahedral structures which are theoretically favored energetically in this regime. For a fixed mole fraction of 0.06, the cluster temperatures, T_c , are systematically higher going from Ar to Xe with dimensionless temperatures, kT_c/ϵ , systematically lower. There is evidence that $P_0 D_0 / (kT_0/\epsilon)$ is the unifying parameter for predicting the onset of massive clustering for rare gases in these nozzle-type sources.

Creation and Structure Study of Vacuum
Isolated Clusters of Argon, Krypton and Xenon

by

Sang Soo Kim and Gilbert D. Stein*
Northwestern University
Gasdynamic Laboratory
Department of Mechanical and Nuclear Engineering
Evanston, Illinois 60201

Abbreviated title

Cluster Structure of Ar, Kr and Xe

February 27, 1981

To appear in the Journal
of Colloid and Interface Science

*Person to whom correspondence should be addressed.

ABSTRACT

Homogeneous clusters of Ar, Kr or Xe are formed in adiabatic, high Mach number expansions through very small, diverging Laval nozzle sources. A He carrier gas is employed and the mole fraction of condensable species varied from 1.0 to 0.06 in an effort to control the cluster size distribution and temperature. The nozzle source is part of a multi-stage molecular beam apparatus. Electron diffraction, using a 40 keV beam, is used to study cluster structure. Cluster sizes are varied from 10^{-5} to 1,500 atoms per cluster and temperatures range from 20 to 60 K. The structure for $1,000$ is bulk f.c.c. and transforms gradually into a non-crystalline structure as size decreases. The smallest structures, for all three noble gases, are consistent with the icosahedral structures which are theoretically favored energetically in this regime. For a fixed mole fraction of 0.06, the cluster temperatures, T_c , are systematically higher going from Ar to Xe with dimensionless temperatures, kT_c/e , systematically lower. There is evidence that $P_{D_0}/(kT_c/e)$ is the unifying parameter for predicting the onset of massive clustering for rare gases in these nozzle-type sources.

Accession For	<input checked="" type="checkbox"/>
NTIS GRA&I	<input type="checkbox"/>
DTIC TAB	<input type="checkbox"/>
Unannounced	
Justification	
BY	
Distribution/	
Availability Codes	
Avail and/or	
Dist	Special
	A

INTRODUCTION

Our research interests have been directed toward the production and study of very small particles or clusters with sizes below 5,000 molecules per particle. This is the very interesting size range in which physical properties begin to deviate from those of bulk material. The use of low density molecular beam techniques permits the study of clusters which do not interact with each other or with a support media such as a solvent, matrix, or substrates. This "splendid isolation" which is theoretically more ideal for research purposes, is achieved at the expense of relatively low sample density. Our primary structure diagnostic technique has been the use of high energy electron diffraction in which a 40-50 keV electron beam crosses the beam of clusters formed in a multi-stage molecular beam source (1-3). Since the particles or "micro crystals" have random orientation in the beam the patterns are of the Debye-Scherrer type. The patterns are used to ascertain the crystal structure and their deviation, if any, from that of bulk lattice configurations. In addition, the particle size is in a size range to cause peak broadening so that an estimate may be made of the mean particle size in these beams. For some materials the variation in peak height from the kinematic theory may be used to determine approximate cluster temperature.

Small clusters arise naturally as an important entity in the treatment of the kinetics of phase change and, in nearly all cases, clusters are formed as the result of a phase change. Thus an interesting interdependence arises in which the physical properties of small clusters are important in theoretical predictions for the kinetics of phase change, and conversely, an understanding of the kinetics of phase change is important for the production of clusters of a given mean size for use in the measurement of their properties.

A variety of species have been investigated in our laboratory. They range from atomic and molecular van der Waals aggregates (4-7), to the more tightly bound (a factor of 20), hydrogen-bonded clusters (3,8), to the yet more strongly bonded (another factor of 20) metal particles (9-11).

The use of small, controlled-expansion Laval nozzle sources for cluster beams, pioneered in Karlsruhe (12-14), has been adopted in this work. Prior research in this laboratory, on the thermodynamics and gasdynamics of very small hypersonic nozzles (6) and on the cluster nucleation kinetics (5), for SF_6 clustering in an Ar carrier gas, provided the experience needed to design nozzles for the present rare gas studies.

The use of a carrier gas is absolutely essential for the study of SF_6 nucleation since its specific heat ratio $\gamma = c_p/c_v$ is so near unity. (c_p and c_v are the specific heats at constant pressure and volume respectively.)

In this work the carrier gas (He) has the same value of γ as the condensable species (Ar or Kr or Xe) so γ is not a factor. However, nucleation research on larger nozzles reveals that the use of a carrier gas will provide colder clusters than pure gas expansions (15) and narrower size distributions. Also, variation of the condensable species mole fraction is another means to vary the spread in size and the cluster concentration. Theoretical solutions to the gasdynamic equations of motion, coupled with a nucleation rate equation and droplet growth law, predict higher concentrations, smaller mean size, and narrower size distribution as condensable mole fraction, X_0 , is reduced. This trend is highly desirable for cluster beam experiments. Of course, if the mole fraction becomes vanishingly small, no significant clustering will occur. The time scale for these expansions is so short, e.g. 1 to 10 μsec , that the cooling rate of the gas is the 10^7 $^\circ\text{C}/\text{sec}$ range and thus the overwhelming majority of clusters formed are pure or homogeneous, in

contrast to heterogeneous clusters nucleated onto surfaces or foreign particles.

Since the pressure in the first pumping stage is well below the exit pressure of the nozzle the mixture will continue its adiabatic expansion beyond the nozzle exit until the density becomes so low that the flow becomes collisionless. This latter part of the flow is essentially uncontrolled and the temperature will continue to drop. Thus there is a tendency for the carrier gas to also supersaturate, with the possibility of binary or heterogeneous nucleation leading to mixed clusters. There is some evidence, thermodynamic as well as electron diffraction, for this in SF_6 -Ar expansions for very specific operating conditions (16). To avoid this problem He is used as the carrier for the noble gas clustering experiments reported here. Because He has relatively high kinematic viscosity, the nozzles had to be designed to compensate for thicker boundary layers (7).

NOBLE GAS CLUSTERS

Several investigators have shown that the structure and properties of very small clusters ($g < 200$ where g is the number of atoms in a cluster) may be significantly different from those of the bulk phase. Recent studies indicate that for small cluster size the minimum energy configurations are icosahedral or dodecahedral, structures which cannot propagate into a regular array for large sizes like the more familiar bulk crystalline structure (17-21). McGinty (22,23), and Burton and Briant (18,24) have performed molecular dynamics studies of the structure and thermodynamic properties of argon microclusters. Monte Carlo computer simulation techniques of classical statistical mechanics have been employed by Lee, Barker and Abraham and other investigators (25-28).

It has been shown experimentally that small Ar clusters in supersonic beams are in a solid state and have a non-bulk type structure when their size is about forty atoms per cluster (29). This structure is a stable one and exists because the formation of the ordered lattice is not energetically favorable for small numbers of atoms in the cluster. Also, in model calculations of a solid microcluster in thermodynamic equilibrium, the diffraction pattern undergoes substantial changes as the number of atoms changes from 50 to 60. This indicates that there exists a transition in which the microcluster changes from the polyicosahedral to the multishell icosahedral structure (29). This means that even ordinary lattice-structural crystallites can grow from the smallest, crystallographically-speaking, amorphous embryos of a few atoms.

Noble gases are studied because realistic interaction potentials are available and theoretical calculations have been restricted almost exclusively to this type of species. The heavier noble gases are included in this study because the range of potential well depth, ϵ , from Xe to Ne is almost a factor of 8. This implies that the Xe structures will be far more rigid or crystalline for a given cluster temperature than Ne or Ar and will have more efficient electron scattering. Molecular dynamics modeling of clusters indicates that the minimum energy configurations are more likely to occur at colder temperatures T (i.e. the lower the value of kT/ϵ , k being Boltzmann's constant). There is, in addition, the possibility of comparing these structures to those of some metals (10).

As mentioned previously, He is used as carrier gas because of its relatively low condensation temperature and also the fact that γ being the highest possible value, $5/3$, enhances the gas cooling during the adiabatic expansion. The use of pure noble gas expansions is also an option but

does not allow the possibility of controlling the cluster size distribution or cluster temperature that is potentially available using a carrier gas. In addition there is the problem of the high cost of pure gases such as Xe.

MOLECULAR BEAM CONFIGURATION

The cluster beam apparatus is shown schematically in Fig. 1. It consists of a conventional, three-stage, differentially pumped molecular beam which enters a scattering chamber where it is crossed by a 40 keV electron beam. The diffraction patterns are obtained using a single-channel, electron-scintillator, photon counting detection system. The molecular beam defining elements are the nozzle, skimmer and collimator. This system is built in an axially concentric configuration.

The supersonic nozzle expansion takes place in the first stage and is pumped with a 10 cm model 150 stokes ring-jet booster pump using Dow Corning 704 diffusion pump fluid. The second chamber is evacuated by a 15 cm diffusion pump using Dow Corning 704 fluid backed with a freon cooled chevron baffle. This pump has a maximum pumping speed of 2000 l/sec and the chamber blank off pressure is 10^{-7} torr. The third stage is the detection chamber 45 cm high x 55 cm x 55 cm constructed of 2.5 cm thick aluminum. This chamber is pumped by two 15 cm diffusion pumps again backed with freon cooled chevron baffles. This pump combination gives a maximum pumping speed of 4,000 l/sec and a chamber blank off pressure of 10^{-6} torr without cryopumping. Using a liquid nitrogen trap, the box pressure goes down to 10^{-7} torr. This chamber contains an ionization gauge for monitoring the molecular beam intensity and the background pressure. The background pressure is obtained by rotating the gauge out of the molecular beam axis.

The electron beam is aligned to cross the molecular beam at a right angle, 7.68 cm downstream from the skimmer orifice and ends at the beam stop.

The accelerating voltage of this electron diffraction unit gives an incident electron beam wavelength of 0.061 Å (10 Å = 1 nm). From the calibration with the gold thin film sample, the distance between the crossing point of the two beams to the diffracted electron beam detecting surface is 26.2 cm.

The axisymmetric Debye-Scherrer diffraction patterns from the cluster beam are measured by a single channel scintillation detection system. This system has been developed in our laboratory because the pursuit of cluster structure in the 10-100 molecules per cluster size range nearly always involves sample densities so low that the scattered electron signal and signal-to-noise are too low for film detection.

The molecular beam is chopped and the scattered electrons that pass through the detector aperture A_d are stopped in a Pilot B scintillator producing 10-100 photons per electron. The photon pulse passes through a fiber optic to a cooled RCA 8575 scintillation counting photomultiplier outside of the vacuum system. An "up-down" counting scheme is designed to count up the signal plus background counts for the half cycle when the cluster beam is open (minus the opening and closing shutter function), and counts down or subtracts background counts for the remaining half cycle when the beam is off.

Laval Nozzle Sources

The three very small diverging Laval nozzles used here are designated Nozzle 11, 12 and 13. They are fabricated from glass capillary tubing. Nozzle 11 and 12 have the same inlet diameter, D_0 , while Nozzle 12 and 13

have the same contour except very close to the nozzle entrance. Nozzle 11 opens up more rapidly than 12 and 13. See Table I and Ref (7) for additional details. The gas mixture, which enters the stagnation chamber ahead of the nozzle, can be cooled with a liquid nitrogen heat exchanger and fine tuned using a resistance heater.

The theoretical description of these nozzle flows is complicated due to the wall viscous effects. They have, nevertheless, been modeled successfully for SV_6 flows (6) and theoretical calculations for the noble gas expansions will be the topic of a future manuscript. Barring a full description of the kinetics of phase change in these nozzles, a relative estimate of the tendency to nucleate clusters can be obtained by computing the total number of binary collisions, N_{coll} , an atom undergoes through the expansion, from the point x_1 where the condensable species saturates to x_2 where the condensable vapor becomes collisionless,

$$N_{coll} = \int_{x_1}^{x_2} s dt = \int_{x_1}^{x_2} \frac{dx}{v} \quad (1)$$

where $s = \bar{v}/\lambda'$ is the collision frequency and $\bar{v} = (8kT/m\pi)^{1/2}$ is the mean thermal (not flow) velocity. The mass per atom is m and $\lambda' = 1/\sqrt{2} n \sigma$ is the mean free path between collisions of condensable species whose number density is n and σ is the condensable species collision crosssection. The time interval dt can be written as dx/v where v is the flow velocity. Assuming the gas is perfect and the flow isentropic one obtains

$$N_{coll} = \frac{4\sigma^2 p_0 D_0}{(2\pi v)^{1/2} k T_0} \int_{x_1}^{x_2} \frac{dx}{x_1} \frac{1}{M(1+\frac{x-1}{2} N^2)^{1/2} (\gamma-1)}, \quad (2)$$

where $x = x/D_0$ is the dimensionless distance through the nozzle and $M = v/a'$ is the Mach number, a' being the local sound speed. The subscript 0 denotes

stagnation conditions, see e.g. Fig. 1. An increase in P_0 , D_0 or X_0 or a decrease in T_0 will increase N_{coll} thus tending to shift the supersaturated flow toward the point of massive clustering, i.e., to the onset of condensation

Molecular Beam Intensity Measurements

The pressure reading of the detection chamber ionization gauge can be converted to the molecular beam flux by the relation (30)

$$I_{\text{(molecules/sec)}} = \frac{K\alpha(P_T - P_B) \times 10^{20}}{(\mu T)^{\frac{1}{2}}} \quad (3)$$

where α is related to the ionization constant for the gas and is 0.66 for Ar, 0.45 for Kr and 0.35 for Xe (31). The total pressure in torr ($750 \text{ torr} = 10^5 \text{ pascal}$) of the molecular beam plus the background measured by the ionization gauge along the beam path is P_T and P_B is the background pressure of the detection chamber in torr. The molecular weight of the gas is μ , and T is the temperature of the gas leaving the ionization gauge. The gauge constant K depends on the geometry of the ionization gauge. Calculation of molecular flow conductance in a circular tube (32) gives a value of $K = 250$ in this experiment. To convert the beam flux to the molecular beam intensity, atoms per cm^2 per second, at the point x_c where the molecular beam is crossed by the electron beam, Eq. (3) should be divided by the beam crosssection at x_c ($A = 0.033 \text{ cm}^2$) obtained from the geometric ratio of the beam defining elements shown in Fig. 1.

Consider now the molecular beam intensities for the three nozzles and $X_0 = 0.06$, Kr in No. Nozzles 11 and 12 have the same inlet diameter D_0 but 11 has a contour that diverges more than 12. Its onset is slightly earlier due to less viscous dissipation and has higher cluster beam intensities up to $P_0 = 6 \text{ Bar}$. Nozzle 13 has a smaller D_0 but the same general contour as 12.

Its onset is delayed to $P_0 = 6 \text{ Bar}$. The integral in Eq. (2) is about the same for the three nozzles so N_{coll} scales with D_0 . When Fig. 2 is re-plotted vs. P_0/D_0 the onsets and growth are nearly all coincident. The effect of T_0 on beam intensities is revealed in Fig. 3 for Nozzle 11 and two $X_0 = 0.06$ mixtures, Kr and Xe. As seen in Eq. (2) N_{coll} increased with decreasing T_0 . The variation is not linear due to boundary layer variations with P_0 and T_0 and thus the integral varies with these quantities. Note that the 3 Bar curves nearly coincide when replotted as a function of the dimensionless temperature KT_0/e . This trend was also noted in a previous paper (7). Once the beam intensity exceeds unity on the a.u. scale (arbitrary but linear scale with 1 a.u. equal to $3 \times 10^{17} \text{ atoms cm}^{-2} \text{ sec}^{-1}$ for Ar, $1.5 \times 10^{17} \text{ atoms cm}^{-2} \text{ sec}^{-1}$ for Kr, and $9 \times 10^{16} \text{ atoms cm}^{-2} \text{ sec}^{-1}$ for Xe at the electron beam location (33)), there is sufficient cluster density to obtain electron diffraction patterns.

ELECTRON DIFFRACTION

The collision of high energy electrons with matter has been used for many years to determine the molecular structure of solids, liquids and gases. The theory of electron diffraction is based on the work originated by de Broglie (34) and Schrodinger (35). A simplified theory for elastic scattering of high energy electrons has been developed by Born (36) and Mott (37). The theory of inelastic scattering was derived by Morse (38). The wave nature of high energy electrons was first verified in experiments on single crystals by Davisson and Germer (39) and the initial experiments on electron diffraction from gases were made by Mark and Wierl (40). Since this early work electron diffraction has evolved into an important technique for the investigation of matter in all its forms. (see e.g. an excellent treatise on the physics of diffraction by Cowley (41)).

The total scattering intensity of an ensemble of atoms associated together as a cluster having random orientation is I_0 and is given as:

$$I_0 = \frac{1}{L^2} \left[\sum_{i,j} f_i f_j \frac{\sin \pi r_{ij}}{\pi r_{ij}} + \sum_i f_i^2 + \frac{2}{a_H} \sum_i \frac{f_i^2}{a_i} \right] \quad (4)$$

where I_0 is the intensity of the incoming electron beam, L is the distance from the scattering volume to the plane of observation, $r_{ij} = |r_i - r_j|$ is the distance between atoms i and j , $s = (4\pi/\lambda) \sin(\theta/2)$, θ is the scattering angle measured from the undeflected electron beam, λ is the de Broglie wave-length given by Eq. [4], $a_H = h^2/(4\pi^2 m_e e^2)$ is the classical Bohr radius of hydrogen where e is the electron charge, h is Planck's constant, m_e is the electron mass, and S_i is the inelastic scattering factor of the i -th atom. The electron elastic scattering factor for the i -th atom is:

$$f_i = \frac{2}{a_H} \left[\frac{Z_i - F_i}{2} \right] \quad (5)$$

where F_i is the x-ray scattering factor and Z_i is the atomic number of the i -th atom. The values of F and S for all atoms are tabulated (42).

The first sum in Eq. [4] is the elastic or coherent interatomic contribution of scattered intensity which gives the Debye-Scherrer type of diffraction patterns on the observation plane. The structural information for the cluster is provided by this term. The second term is the coherent atomic contribution and the third term is the incoherent or inelastic atomic contribution. Both the atomic sums decrease rapidly with increasing scattering angle, with the decrease of the incoherent intensity being greater than that of the coherent atomic intensity.

Considering the scattering from N clusters with no positional correlation and taking into account the damping term due to thermal vibrations in a cluster, i.e., the Debye-Waller factor $\exp(-s^2 \langle u^2 \rangle / 3)$,

$$I_0 = \frac{N I_0}{L^2} \left[\sum_i \sum_j f_i f_j \frac{\sin \pi r_{ij}}{\pi r_{ij}} e^{-s^2 \langle u^2 \rangle / 3} + \frac{2}{a_H} \sum_i \frac{f_i^2}{a_i} \right] \quad (6)$$

The mean square displacement $\langle u^2 \rangle$ is a function of temperature and Debye temperature θ

$$\langle u^2 \rangle = (424/m) (T/\theta^2) [\theta/4T + 9(\theta/T)] \quad (7)$$

where $\langle u^2 \rangle$ is expressed as \AA^2 , the temperature as degrees Kelvin and m is the atomic mass. The function between brackets is calculated for each value of θ/T (see Table I).

The finite extent of the long range order of a crystalline cluster has been shown by Scherrer (43) to result in a broadening of each of the Bragg peaks proportional to the cluster size for small clusters where the small size alone, of an otherwise perfect crystal, can be considered as a crystal imperfection resulting in incomplete diffraction by the scattered electrons. The Scherrer formula is:

$$\lambda = \lambda L / (\delta^2 - \delta_0^2)^{1/2} \quad (8)$$

where λ is the characteristic length of the cluster and δ and δ_0 are the full width of the half maximum height of the intensity peaks of the sample and the reference material (polycrystalline Au thin film with size greater than 100 \AA , i.e., the instrumental line broadening). This is valid for crystals less than 100 \AA in diameter. For crystals larger than 100 \AA the peak broadening effect is too small to be observable (44). Assuming the clusters are spherical, this length would be a diameter, d , and is an averaged value over the range of sizes present in the molecular beam. The "average" number of atoms per cluster, \bar{n} , can be estimated by the formula

$$\bar{n} = \frac{d^3}{6} \cdot n \quad (9)$$

where a is the unit cell dimension, d is cluster diameter and n is the number of molecules in a unit cell (in case of f.c.c., $n=4$).

Interpretation of Electron Diffraction Patterns

As mentioned before, the main goal of this investigation is to determine the differences in structure of very small clusters, from that of the bulk phase, as the average size is diminished. The size at which changes occur, as well as the nature of these changes, is of importance. Therefore most of the electron diffraction patterns in this experiment have been taken under conditions for production of small clusters, i.e., relatively weak beam intensities. Although the cluster size is varied continuously, it is useful to consider two regimes of cluster size. Without exception, when the clusters are large ($\bar{g} = 10^3$ to 10^4 molecules/cluster), their diffraction patterns show all the characteristic lines of a bulk crystalline structure (45). As a first approximation, the crystalline properties of clusters can be defined following the standard methods for cluster size, unit cell dimension and peak intensity. However, as the cluster size approaches the $\bar{g} = 10$ to 10^2 regime, the pattern begins to vary appreciably from the standard unit cell structure. Even for the case where the unit cell structure is constrained (theoretically) to remain the same as bulk, the diffraction patterns vary greatly. It is estimated that about 60 unit cells are required to produce bulk type diffraction patterns (46). In this case, the use of models and the calculation of their diffraction functions becomes indispensable.

The typical electron diffraction patterns of Ar clusters of large size ($\bar{g} \approx 1,000$ molecules/cluster) and small size ($\bar{g} \approx 220$ molecules/cluster) are shown in Figs. 4 and 5. The peaks of the f.c.c. structure become less and less resolved as size is decreased. Diffraction patterns of Kr and Xe

clusters are shown in Figs. 6 and 7. The intensities of diffraction patterns are plotted in arbitrary units (a.u.) and can be converted to electron counts using I_{exp} (counts/sec amp incoming electron beam) = I_{exp} (a.u.) $\times 10^7$. A typical beam current is 5 μ A.

The peaks for the icosahedral structure are simply numbered consecutively since there are no set of Miller indices defined for this non-periodic cluster configuration. Details of this structure are given in the next section.

The average crystallite diameter, d , is estimated by using the Scherrer formula given by Eq. (8). The width of the 111 and 220 peaks are used to estimate d . However, in the case of small clusters where the widths of the 220 and 311 are positioned too close to be separately resolved, only the width of the 111 peak is used. The formula of Scherrer gives a precision better than 20% on the diameter estimation and this uncertainty is of the same order of magnitude as the estimated width of the size distribution in the cluster beam. The results are presented in Fig. 8. The sizes appear in the order Xe, Kr and Ar with increasing p_0 , or partial pressure of the condensable species since $X_0 = 0.06$ for all mixtures, as expected. The number of atoms per cluster, \bar{g} , is obtained with Eq. (9) and is shown in parenthesis for the Nozzle 11 data. The range in \bar{g} is from 50 to 1,500.

Since electron diffraction patterns from very small clusters ($\bar{g} < 1,000$ molecules) no longer exhibit well-defined peaks and most of the clusters investigated, except pure Ar, present a non-crystalline arrangement which becomes predominant with decreasing cluster size, the estimation of the lattice parameter has a greater uncertainty. This implies that perhaps a number of characteristic interatomic dimensions, of nearly the same length, are partially responsible for the broadening.

MODEL CALCULATION

When the average size of the clusters decreases, the crystalline lines become less and less resolved and in general the diffraction patterns yield less and less information. The construction of the appropriate cluster models must be used in place of the conventional crystallographic approach. Using diverse types of models, crystalline or non-crystalline, one can describe or at least approach the experimentally obtained structure of clusters in the beam.

There are two kinds of methods used to investigate the structure of micro-clusters which do not exhibit normal bulk-like packing of atoms. One method, of determining the particular structure of a non-crystalline solid, is to calculate the radial distribution function (RDF) from the model cluster and compare this RDF with experimental RDF which is obtained by taking the Fourier sine transform of experimental intensity data. Investigations of the structure of amorphous materials traditionally proceed in this manner.

Another method is comparison of the observed interference function, $I_{\text{exp}}(s)$, with theoretical interference functions, $I_{\text{th}}(s)$, for a variety of atomic models. Since the coordinates of the model are known, $I_{\text{th}}(s)$ can be calculated exactly with the Debye formula (Eq. [6]). The average local atomic order will then be described by the atomic model which matches $I_{\text{exp}}(s)$ with the best fit. The advantage in using the interference function for this purpose should be emphasized, since the difficulties in obtaining a reliable RDF from the experimental data are thereby avoided. Thus this latter method is used here.

The uniqueness of the assumed model, which is found to agree with an observed diffraction pattern, can be tested by determining the magnitude of

the variation of the parameters for the model which can be tolerated, while still retaining agreement with the recorded data to within the experimental error. The possibility that radically different structures may lead to the same intensity pattern (homomeric structure) has been discussed by Patterson (47). He concludes that it is difficult to prove uniqueness.

Calculation of Interference Function $I(s)$

The Debye formula, Eq. [6], will be utilized. For the g atoms of the cluster, the time-averaged intensity, expressed in electron units, becomes

$$\begin{aligned} I(s) = g^2 (1 - s^2 u^2) + s^2 u^2 \left[\sum_{i=1}^g \sum_{j=1}^g e^{2\pi i s \cdot r_{ij}} \right] \\ + \sum_{i=1}^g \frac{s_i(s)}{s} \end{aligned} \quad [10]$$

where u^2 is the time-averaged mean square displacement. It is noted that the value of u^2 is different from that of $\langle u^2 \rangle$ viz. $u^2 = \frac{1}{3} \langle u^2 \rangle$, and $2M - s^2 u^2$ in Table I.

When g is small, i.e., the case of a simple molecule, it is possible to determine these parameters adjusting the diffraction function $I(s)$ to the experimental diffraction pattern by the method of least squares. A cluster of a few hundreds of atoms is a problem, since the great number of parameters makes such determination impossible, even if the crystalline symmetries makes an important reduction of this number. Therefore the visual comparison between the diffraction functions calculated from models and the experimental patterns is used and the parameters determined by successive approximations.

When a "static" model is used, the interatomic distances can be calculated from the position of atoms in the model. In particular, the

crystalline models utilized are not relaxed and the atoms occupy the same sites as in the infinite crystal. For the atomic displacement u_{ij} , we do not differentiate the movements of atoms on the surface from those of internal atoms, and we consider that the movement of an atom is isotropic around an average position.

The effects of multiple scattering, as estimated using the two-beam theory of Blackman (48) and Fujimoto (49), are negligible for clusters in the small size range encountered here. Use of the Blackman theory, in the analysis of diffraction patterns for large clusters of Pb ($\bar{g}=2,000$ to 9,000), gave appreciable changes to some peak intensities and resulted in a rational and self-consistent interpretation of the data (10). A more recent theoretical treatment (50) of this problem predicts multiple scattering effects which are approximately an order of magnitude greater than the earlier (48,49) estimates. The effect is still negligible for the lower atomic weight clusters but could be of significance for the larger Xe sizes. A full n-beam treatment, for the random orientation case, would be a formidable undertaking (51) and has therefore not been attempted in this analysis.

Proposed Models

Models of microclusters are proposed by numerous investigators and most of them are for amorphous solids. There are several review papers for structural modeling of disordered semiconductors and amorphous films, e.g., Paul, et al. (52), Chaudhari, et al. (53), Cargill (54) and Hoare (55). Barker (56) also described the main type of clusters that either have been used or could be used to model small monatomic systems at low temperatures. Hoare, Pal and Holmes (57,58,59) have systematically enumerated minimum

energy configurations for clusters of from three to sixty atoms using Lennard-Jones potentials. They found three particular compact non-crystallographic growth schemes, with tetrahedral, pentagonal, and icosahedral symmetries, which were appreciably more stable than f.c.c. microcrystals having the same numbers of atoms. All of the lowest energy clusters obtained by Hoare and Pal (59) correspond to packing of approximately regular tetrahedra (atoms at tetrahedral vertices) face to face. Although high-density (low-energy) clusters can be produced by such tetrahedral packing, they cannot be extended indefinitely, because a tetrahedron is not quite a space-filling object. The f.c.c. crystalline packing corresponds to packing tetrahedra and octahedra. Burton (17,18) and McGinty (22,23) investigated the thermodynamic properties of very small clusters of Ar atoms by molecular dynamics calculations. Briant and Burton (60) have also proposed that the 13-atom icosahedron is an important structural unit in amorphous closed-packed materials.

The Cuboctahedron - f.c.c.

This structure is the well known, compact, face centered cubic structure and the bulk crystal structure of rare gases. One can obviously cut a small assembly of atoms out of a crystal lattice and thus form clusters of greatly varying surface geometries. An example which is somewhat spherical is the 561 - atom f.c.c. cluster, i.e., a closed-five shell cuboctahedron, shown in Fig. 9.

The Icosahedron

Due to numerous theoretical predictions, as minimum energy configurations, the icosahedral structure is a strong candidate for the model of microclusters of rare gases and the closed shells of 13, 55, 147, 309 and 561 atom icosahedrons are therefore used in this analysis.

This smallest set of icosahedral particles consists of a central atom plus one to five shells and is shown in Fig. 10.

Since the unit which occurs repeatedly in the structure is a distorted tetrahedron, which is one twentieth of an icosahedron, the packing densities of the icosahedral shell packing (ISP) is 0.72395 which is smaller than that of cubic closed packing or f.c.c. (0.74048). The limiting packing density for large icosahedra is 0.68018 which is higher than that for body-centered cubic packing (0.68017) but lower than that for cubic closed packing f.c.c. (81). This makes it unlikely that large numbers of atoms might be found arranged as icosahedra.

COMPARISON OF EXPERIMENTAL AND MODEL DIFFRACTION PATTERNS

In order to find best fitting models for small clusters, the peak positions and the peak intensities for the model and experimental diffraction functions are compared. In the case of cuboctahedra, the position of each peak is independent of cluster size, but vary with size for icosahedra.

The cluster model to be compared with experiment contains a mole fraction of free atoms X_f , in addition to the microcrystal fraction which may be a combination of bulk f.c.c., X_{cub} , and icosahedral structure, X_{ico} . The free atom portion can in principle be condensable species and He carrier. The molecular beam pressure is high enough at the skimmer to cause a shock-like interference preferentially scattering He out of the beam (see e.g. Ref. (62)). In addition, the electron scattered intensity goes like f^2 , which is proportional to Z^2 , giving a reduction for He by a factor of 10^3 for Ar to 10^3 for Xe. The gas contribution to the diffraction pattern is therefore taken as due to the condensable species only. Also,

since the cluster beam is chopped, in synchronization with the up-down counter, the effect of background gas scattering is greatly diminished.

Once the coordinates of each atom are determined, there are three variables in the theoretical description. These are M in the Debye-Waller factor e^{-2M} , the portion of the free atoms in the beam X_f and atomic diameter $d_a(\text{\AA})$ as a nearest neighbor distance.

The calculated diffraction patterns of cuboctahedral and icosahedral structures are shown in Figs. 11 and 12 respectively, for Ar clusters ($g=13, 55, 147$ and 309). In order to show the patterns clearly for the high s values, $1/g^2$ is plotted instead of I , $X_f=0$, and the cluster temperature is 0 K ($B=0.85$). As expected, when the number of atoms in the cluster increases, more peaks are resolved and the shape of the peaks are sharper and taller. In both cases, almost every peak has clearly appeared when $g>147$. In the case of cuboctahedra, we can distinguish the 200 peak from the 111 near $s=2\text{\AA}^{-1}$ and the 422 from the 333 near $s=6\text{\AA}^{-1}$, when $g>147$. Between the curves of $g=13$ and 55, the second peak is divided into two (220, 311) and the 400 peak starts to appear at $s=4.70\text{\AA}^{-1}$ when $g=55$.

Consider the differences between the two structures in the case of $g=147$. First notice that the two curves are very different in appearance, especially the third and the fourth peaks ($3<s<4$). In the case of icosahedra, the positions of these peaks are much closer than those of cuboctahedra and there is a small shoulder near $s=3\text{\AA}^{-1}$. Second, the 111 icosahedron peak is greater than that of the cuboctahedron by a factor of 1.3 for a given g . It is also seen that the second peak is much smaller and the separation from the first peak is much clearer in the icosahedral structure.

The theoretical diffraction pattern for a single icosahedron of Ar, Kr and Xe is seen in Fig. 13 for $g=147$, $X_0=0$ and $T_c=0$ K. The ratio of the intensities of 111 peaks for Xe, Kr and Ar is 5.8 to 2.4 to 1 and they are shifted to progressively higher s .

Pure Ar

The experimental diffraction functions I_{exp} for Ar clusters formed without He carrier gas are compared with the calculated diffraction functions I_{th} . Pure Ar expansions produce large cluster sizes with patterns that agree well with bulk f.c.c. calculations. The large Ar cluster size is well known to be face centered cubic and the I_{th} are calculated from the cuboctahedra models ($g=309$ and 147). As a result of extensive comparisons of the ratios of the experimental and the theoretical intensities, the best fitting results are summarized in Table II.

From this table, most of the weak patterns (total ionization gauge beam intensity I_b is less than 4 a.u.) show the mixed patterns of the icosahedral and cuboctahedral structures. Even in the case of strong beam intensity (Exp. No. 9/27/79A, $I_b=8$ a.u.) the experimental pattern is very well matched with a mixed pattern having 24% of the beam atoms as icosahedral clusters, 56% of the beam atoms as cuboctahedral clusters and 20% of the beam atoms as free atoms ($g=309$). These results confirm that the structure of very small Ar clusters are not the perfect f.c.c. structure and that as the size becomes smaller there is an increasing portion of icosahedral structure.

These results also explain the anomalously large 111 peak and small 400 peak, in comparison with a perfect f.c.c. cluster. The height of the 111 peak is closely connected with the proportion of the nearest-neighbor distances present. If this peak is found to be too high, it can only be because additional "nearest-neighbor distances" have been introduced in

some way, presumably through atoms occupying close-packed, but non-f.c.c. sites.

Ar in He Carrier Gas

It is generally known that the expansion of a condensable vapor with light scatter gas is much more effective for the production of very small clusters because of the fast expansion rate and the cold cluster temperatures. Figure 14 is an example of an experimental diffraction pattern for $X_0=0.06$ for Ar in He and the best fitting calculated diffraction function. The values of I_{exp}/I_{th} are shown in Table III for several experiments having $X_0=0.06$ and 0.125 and 0.15 for 25% Ar in He carrier gas. In cases of 6% and 17.5% Ar, the experimental results correspond to the icosahedral structures. For the diffraction patterns for the 25% Ar from high intensity cluster experiments ($I_b=8$ a.u.) show mixed patterns of cuboctahedra and icosahedra. It is again noticed that the cuboctahedron portion in the beam increases as the cluster beam intensity, I_b , increases. The temperature of Ar clusters ranges between 20 K and 40 K.

Kr in He Carrier Gas

An example of an experimental diffraction pattern and the best-fitting calculation for Kr clusters produced from a 6% Kr in He mixture is shown in Fig. 15 and the values of I_{exp}/I_{th} the peaks in several experiments are shown in Table V. Most of the experimental results look like the 147 atom icosahedral structure and the cluster temperatures are between 20 K and 60 K, with most of the results near 50°K. The fraction of the free atoms is 30 to 50% in the cluster beam. Even though the beam intensity is relatively high ($I_b=10$ a.u.), the Kr cluster structure is icosahedron.

Xe in He Carrier Gas

A comparison of experimental and calculated patterns for Xe clusters

from 6% Xe in He carrier gas is presented in Fig. 16. The summary for other Xe experiments is given in Table VI. The experimental structures of Xe clusters are best fitted with patterns using 147 and 309 atom icosahedra, similar to the results from 6% Ar and 6% Kr. The strongest Xe pattern among those presented in Table VI (Exp. No. 9/18/798, $P_0 = 5$ bar, $T_0 = 22.4^\circ\text{C}$, $I_0 = 20$ a.u.), has a best fitting model which is the 309 atom icosahedral structure with $X_f = 0.4$ and $T_0 = 40$ K. Knowing $d = 26.8$ Å, obtained from the first experimental peak width, and using the packing density for a four shell icosahedron, 0.69053, the average number of atoms per cluster is 317. (a value quite similar to that of Kr with the same value of I_0). All of the experimental patterns of Xe clusters obtained are for small size clusters - (less than 320) and have icosahedral structure. The range of cluster temperature is 40 to 60 K.

In conclusion, most of the clusters formed from low mole fraction mixtures are three shell or four shell icosahedral structures, or partially filled four shell, depending on the stagnation condition (P_0 and T_0). Increasing the mole fraction of condensable gas (in case of Ar) and/or increasing the stagnation pressure P_0 and/or lowering the stagnation temperature T_0 , i.e., increasing W_{coll} in Eq. [2], increases the portion of f.c.c. structure.

SUMMARY AND CONCLUSIONS

To produce more intense cluster beams, in an interesting size range, three new diverging Laval nozzles (11,12,13) have been designed which diverge more rapidly and have smaller throat diameters and shorter lengths than nozzles used previously to study clustering of molecular species such as SF₆. In spite of the increased effect of He boundary layers within the

nozzle and the finite pumping capacity of our system, these newly designed nozzles work more effectively as cluster sources than either free jets or the older Laval nozzles (i.e., longer length and smaller divergence angle). Using these new beam sources, the scattering chamber remains at high vacuum ($P_{\text{box}} \leq 10^{-6}$ torr) while running the gas at sufficiently high beam intensities to obtain electron diffraction patterns ($I_0 \geq 1$ a.u.).

Lowering the stagnation temperature T_0 is more effective for producing strong molecular beam intensities than raising P_0 when limited pumping capacity is a constraint. This is because the nozzle mass flow rate goes as $P_0^{1/2}$ and $T_0^{-1/2}$. Thus for example, in Fig. 3, reducing T_0 from 200 to -500 for Xe, $P_0 = 3$ bar, increases the mass flow rate by 14%. For the same Xe mixture at 3 bar and 200, P_0 must be increased to 4.5 bar to get the same beam intensity as lowering T_0 above. This causes a 50% increase in mass flow rate, as seen in Figs. 2 and 3, and provides evidence that the parameter $P_0^{1/2}/(RT_0/e)$ may provide a means for unifying the onset of condensation in these Laval nozzle sources.

The diffraction patterns have been obtained using a 40 keV high energy electron diffraction unit and a single-channel, scintillation detection system. Synchronous detection or up-down pulse counting is used to overcome the signal-to-noise limitations associated with beams that contain very small clusters. Cluster size has been calculated from the experimental diffraction patterns with \bar{g} ranging from 1500 down to 50, with the emphasis on beams having less than 500 atoms per cluster. Differences are easily seen between the experimental diffraction patterns and bulk f.c.c. structure. The specific nature of the structural changes are not so easily obtained. In spite of relatively weak beam intensities, well resolved peaks are seen up to $s = 6.3$ Å⁻¹ where significant differences occur.

To find the structure, two models, cuboctahedron and icosahedron, are

employed. The electron diffraction functions are calculated from these models with several variable parameters: the number of atoms per cluster S , cluster temperature (Debye-Waller factor H), nearest neighbor atomic spacing d_0 and fraction of free atoms in the beam X_f . The four smallest closed shell configurations are used: 13, 55, 147 and 309 atoms per cluster. To facilitate comparison of diffraction patterns, the peak intensities have been normalized to the 311 peak and the values of $I_{\text{exp}}/I_{\text{th}}$ tabulated. Cluster temperatures are estimated to be as low as 20 K up to about 60 K.

The agreement between theory and experiment is considered quite good. Many of the theoretical patterns fit the experimental peaks to within a few per cent with most results within 10%. The diffraction patterns of the smallest clusters, for all three noble gases, are consistent with the multi-shell icosahedral structure, with increasing f.c.c. contribution as size increases.

ACKNOWLEDGMENTS

The authors are pleased to acknowledge the partial financial support from the Engineering Energetics Program of the National Science Foundation and the Chemistry Division and the Power Branch of the Office of Naval Research.

REFERENCES

1. Audit, P., and Rouault, M., *Compt. Rend.*, Vol. 265, p. 1100 (1967).
2. Fargas, J., Raoult, B., and Torchet, G., *J. Chem. Phys.*, Vol. 59, p. 3454 (1973).
3. Stein, G. D., and Armstrong, J. A., *J. Chem. Phys.* 58, 1999 (1973).
4. DeBoer, B. G., Kim, S. S., and Stein, G. D., *Rarefied Gas Dynamics*, ed. A. Campargue, Commissariat A L'Energie Atomique, Paris, p. 1151 (1979).
5. Abraham, O., Kim, S. S., and Stein, G. D., to appear in *J. Chem. Phys.* (1981).
6. Abraham, O., Binn, J. H., DeBoer, B. G., and Stein, G. D., to appear in *Physics of Fluids* (1981).
7. Kim, S. S., Shi, D. C., and Stein, G. D., *Rarefied Gas Dynamics*, ed. S. S. Fisher, AIAA, New York, N.Y. (1981).
8. Armstrong, J. A., and Stein, G. D., *Rarefied Gas Dynamics*, ed. K. Karimchahi, Academic Press, New York, p. 279 (1974).
9. Yokosaki, A., and Stein, G. D., *J. Appl. Phys.* 49, 2224 (1978).
10. Yokosaki, A., *J. Chem. Phys.*, Vol. 68, p. 15 (1978).
11. DeBoer, B. G., and Stein, G. D., to appear in *Surface Sci.* (1981).
12. Hagena, O. F., and Obert, W., *J. Chem. Phys.*, Vol. 56, p. 1793 (1972).
13. Hagena, O. F., *Molecular Beams and Low Density Gas Dynamics*, ed. P. F. Wegener, Marcel Dekker, New York (1974).
14. Obert, W., *Rarefied Gas Dynamics*, ed. R. Campargue, Commissariat A L'Energie Atomique, Paris, p. 1181 (1979).
15. Wegener, P. F., *Nonequilibrium Flows*, Vol. 1, Part I, ed. P. F. Wegener, Marcel Dekker, New York (1969).
16. Kim, S. S., and Stein, G. D., *J. Appl. Phys.* 51, 6419 (1980).
17. Burton, J. J., *Cat. Rev. Sci. Eng.*, Vol. 2, p. 209 (1974).
18. Burton, J. J., *J. Chem. Phys.*, Vol. 52, p. 345 (1970).
19. Burton, J. J., *Nature*, Vol. 228, p. 335 (1971).
20. Hoare, M. R., and Pal, P., *Nature Phys. Sci.*, Vol. 230, p. 5 (1971).
21. Hoare, M. R., and Pal, P., *ibid.*, Vol. 236, p. 35 (1972).

43. Scherrer, P., *Z. Physik.*, Vol. 19, p. 23 (1918).
44. Cullity, B. D., *Elements of X-ray Diffraction*, Addison-Wesley, Reading, Mass. (1967).
45. Torchet, G., "Structure et Propriétés Physiques des Aggregats Formes par Detente en Jet Libre des Gaz H_2 , O_2 , CO_2 , H_2O ", Thesis, University de Paris, Sud Centre, D'Orsay (1978).
46. Morozumi, G., and Rittter, H. L., *Acta Cryst.*, Vol. 6, p. 588 (1953).
47. Patterson, A. L., *Phys. Rev.*, Vol. 65, p. 195 (1944).
48. Blackman, M., *Proc. Roy. Soc. London* 173, 68 (1939).
49. Fujimoto, F., *Z. Naturforsch.* Teil A 16, 367 (1965).
50. Bartell, L. S., Raoult, B., and Torchet, G., *J. Chem. Phys.* 66, 5387 (1977).
51. Cowley, J. M., private communication.
52. Paul, W., and Connell, G.A.M., *Physics of Structurally Disordered Solids*, ed. S. S. Mitra, pp. 45-91, Plenum Press, New York/London (1976).
53. Chaudhuri, P., Graczyk, J. P., and Ward, S. R., *Physics of Structurally Disordered Solids*, ed. S. S. Mitra, pp. 31-43, Plenum Press, New York/London (1974).
54. Cargill III, G. S., *Ann. M. Y. Acad. Sci.*, Vol. 279, p. 208 (1976).
55. Hoare, M., *ibid.*, Vol. 279, p. 186 (1976).
56. Barker, J. A., *J. de Physique, Colloque C2, Tome 38*, C-37 (1977).
57. Hoare, M. R., and Pal, P., *Adv. Phys.*, Vol. 24, p. 645 (1975).
58. Hoare, M. R., and McInnes, J., *Faraday Discussion of Chem. Soc.*, Vol. 61, p. 12 (1976).
59. Hoare, M. R., and Pal, P., *Adv. in Phys.*, Vol. 20, p. 161 (1971).
60. Briant, C. L., and Burton, J. J., *Phys. Stat. Sol.* (b), Vol. 85, p. 393 (1978).
61. Mackay, A. L., *Acta Cryst.*, Vol. 13, p. 916 (1962).
62. Becker, E. W., Klingelhöfer, R., and Lohse, P., *Z. Naturforsch.*, Vol. A17, p. 432 (1962).

22. McGinty, D. J., *Chem. Phys. Letter*, Vol. 13, p. 525 (1972).
23. McGinty, D. J., *J. Chem. Phys.*, Vol. 58, p. 4733 (1973).
24. Briant, C. L., and Burton, J. J., *ibid.*, Vol. 63, p. 2045 (1975).
25. Lee, J. K., Barker, J. A., and Abraham, F. F., *ibid.*, Vol. 58, p. 3166 (1973).
26. Abraham, F. F., *ibid.*, Vol. 72, p. 359 (1980); *ibid.*, Vol. 72, p. 1412 (1980); *ibid.*, Vol. 50, p. 3977 (1969).
27. Abraham, F. F., and Dave, J. V., *ibid.*, Vol. 55, p. 4817 and p. 1587 (1971).
28. Teat, N. H., Abraham, F. F., and Pound, G. M., *Surf. Sci.*, Vol. 77, p. 465 (1978).
29. Farges, J., de Feraudy, M. F., Raoult, B., and Torchet, G., *J. Phys. (Paris)* No. 7, Tome 38, C2-47 (1977).
30. Fenn, J. B., and Deckers, J., *Rarefied Gas Dynamics*, ed. J. A. Laumann, Academic Press, New York, Vol. I, p. 497 (1963).
31. Redhead, P. A., Hobson, J. P., and Kornelsen, E. V., *The Physical Basis of Ultrahigh Vacuum*, Chapman and Hall Ltd., London, pp. 264-265 (1968).
32. *Veeco's Vacuum Products 1977 Catalog*, Veeco Instrument Inc., New York, p. 167 (1977).
33. Kim, S. S., "A Study of the Formation and Structure of Small Clusters of Noble Gases and Sulfur Hexafluoride Formed in Laval Molecular Beams," Ph.D. Thesis, Northwestern University, Evanston, Illinois (1980).
34. de Broglie, L., *Phil. Mag.*, Vol. 47, p. 446 (1924).
35. Schrödinger, E., *Ann. Physik.*, Vol. 79, p. 361 (1926).
36. Born, M., *Z. Physik.*, Vol. 38, p. 803 (1926).
37. Mott, N. F., *Proc. Roy. Soc. (London)*, Vol. 127, p. 658 (1930).
38. Morse, P. M., *Z. Physik.*, Vol. 33, p. 433 (1932).
39. Davison, C. J., and Gerner, L. H., *Phys. Rev.*, Vol. 30, p. 705 (1927).
40. Mark, H., and Wierl, R., *Naturwiss.*, Vol. 18, p. 205 (1930).
41. Cowley, J. M., *Diffraction Physics*, North-Holland, Amsterdam (1975).
42. *International Tables for X-ray Crystallography*, eds. C. H. MacGillivray and G. D. Rieck, Kynoch Press, Birmingham, England, Vol. III (1962); *ibid.*, eds. J. A. Ibers and W. C. Hamilton, Vol. IV (1973).

FIGURE CAPTIONS

- Figure 1. A schematic of the molecular beam system is shown, where M - nozzle, S - skimmer, C - collimator, E.B. - electron beam, M.B. - molecular beam, I.G. - ionization gauge, DT - beam trap, A_d - detector aperture, Sc - scintillator, and PMT - photomultiplier. x_{n-g} is the distance between nozzle exit and skimmer orifice, and is variable.
- Figure 2. Beam intensities for Kr, as a function of P_0 , are shown for Nozzle 11, 12, and 13 at room temperature $T_0 \approx 295$ K and $X_0 = 0.06$ in a He carrier gas. When plotted vs. P_0 , the Nozzle 13 data shifts as indicated by the arrow.
- Figure 3. Beam intensities for Kr and Xe, as a function of T_0 , are shown for Nozzle 11 with several P_0 . The temperature, non-dimensionalized with the interatomic well depth ϵ , provides a means of unifying the noble gas data.
- Figure 4. A high \bar{g} electron diffraction pattern is shown for Ar clusters at $P_0 = 8$ bar and $T_0 = 233$ K obtained with the single channel detection system. The beam is chopped at 100 Hz and the net signal accumulated for 5 sec at each discrete detection angle ($s = (2\pi/\lambda) \sin(\theta/2)$).
- Figure 5. An electron diffraction pattern for 6% Ar in He at $P_0 = 8$ bar and $T_0 = 233$ K for Nozzle 11 is shown. This pattern is different from the regular face-centered-cubic pattern and the symbols $\bar{1}$, $\bar{2}$, $\bar{3}$, etc., indicate consecutive peaks from the theoretical icosahedral diffraction pattern.
- Figure 6. An electron diffraction pattern for 6% Kr in He for Nozzle 11 at $P_0 = 4$ bar and $T_0 = 220$ K is shown. This pattern is also different from that of f.c.c. structure.

- Figure 7. An electron diffraction pattern for 6% Xe in He is shown for Nozzle 11 at $P_0 = 4$ bar and $T_0 = 273$ K.
- Figure 8. The average cluster size for Ar, Kr, and Xe, as obtained from $\bar{N} = 8j$, is shown as a function of P_0 for Nozzle 11 and 12 with \bar{g} given in parenthesis for Nozzle 11 using Eq. [9].
- Figure 9. Structures of cuboctahedron are shown: a) a 13 atom cuboctahedron and b) a 561 - atom cuboctahedron f.c.c. cluster (after Barker (56)).
- Figure 10. a) A 13-atom icosahedral cluster. b) The smallest of the icosahedral clusters containing 13, 55, 147, 309 and 561 atoms. (after Barker (56)).
- Figure 11. Calculated diffraction functions of Ar cuboctahedra ($N = 13, 55, 147$ and 309) are shown. The ordinate I/g^2 is plotted to show the peaks at higher s more clearly.
- Figure 12. Calculated diffraction functions of Ar icosahedra ($N = 13, 55, 147$ and 309) are shown.
- Figure 13. I_{th} of 147-atom icosahedra of Ar, Kr and Xe with no free atoms are shown at $T_0 = 0$ K. Each peak is numbered consecutively.
- Figure 14. A comparison of theoretical model to experiment, I_{th} to I_{exp} is presented for 6% Ar in He. (See Table III for additional details.)
- Figure 15. I_{th} and I_{exp} for 6% Kr in He are compared. (See Table V for details.)
- Figure 16. I_{th} and I_{exp} for 6% Xe in He are compared.

TABLE I
B Values for the Debye - Waller Factor e^{-2M} a)
 $B = \left(\frac{11492T}{m \theta^2} \right) \phi(\theta/T) + \frac{2873}{m \theta} \quad \text{Å}^2$ b)

Cluster Temperature T_c, K	Ar $m = 40, \theta = 85$	Kr $m = 83.8, \theta = 63$	Xe $m = 131.8, \theta = 55$
0	0.85	0.54	0.40
10		0.63	0.413
20	1.14	0.86	0.69
30	1.45	1.15	0.95
40	1.79	1.47	1.22
50	2.14	1.80	1.49
60	2.54	2.13	1.77
70	2.92	2.47	2.06
80		1.80	2.34
90		3.25	2.72
100		3.49	2.91
110		3.83	3.20
120			3.48
130			3.77
140			4.06

a) $M = 8 \pi^2 \frac{u^2}{\lambda^2} \sin^2(\theta/2) = 8 \frac{\sin^2(\theta/2)}{\lambda^2}$
b) ϕ is the Debye characteristic temperature and T is the absolute temperature.
Values of $\phi(x)$ are given in International Tables for X-ray Crystallography. (42)

TABLE II
The Best Fitting Models for Ar Cluster

Experiment No.	Experimental Conditions P_0 (bar) T_0 (K) I_p (a.u.)	Cluster Size (Å)	Models a) X_{ico} X_{cub} X_f N_s b) T_c (K)	I_{exp}/I_{th} 1st (200) 2nd (220) 3rd (311) 4th (400) 5th (331+420) 6th (331+420)
Nozzle 11	297 45	29.8	0.24 0.56 0.2 4	1.00 0.96 1.04 1.00 1.00
7/6/79C	8	31.3	0.32 0.48 0.2 4	1.00 0.94 1.00 0.98 1
12/10/79B	7	32.6	0.14 0.56 0.3 3	1.03 0.97 1.03 0.99 1
1/24/80B	8	34.6	0 0.5 0.5 4	1.04 0.84 0.92 0.95 1
Nozzle 12	9	57.5	0 0.8 0.2 4	1.03 0.88 0.99 1 0.97
9/27/79A	9	295	0.24 0.56 0.2 4	1.00 1.00 1.06 1 0.97
Nozzle 13	5	25.8	0.4 0.4 0.2 4	1.06 0.80 0.96 1 1.00
2/13/80B	5	27.4	0.24 0.56 0.2 4	0.97 0.97 0.98 1 1.00
2/13/80C	7	27.4	0.16 0.64 0.2 3	1.10 1.005 0.96 1 1.00
3/20/80B	5	26.2	0.48 0.1 0.2 4	0.99 1.00 0.95 1 0.92

a) X is the mole fraction of each structure in the beam.
b) N_s is the number of shells of the model clusters.
($N_s = 1 + N = 13$, $N_s = 2 + N = 55$, $N_s = 3 + N = 147$, $N_s = 4 + N = 309$)
c) I_{exp} and I_{th} are normalized by I_{311} in each case.
d) In case of fcc structure, the peaks of the diffraction functions are numbered consecutively.
However, the peaks are indexed in case of cuboctahedron.

Table III

The Best Fitting Models for Ar Clusters from 6% and 12.5% Ar - He Mixtures^{a)}

Experiment No.	Experimental Conditions			Cluster Size (Å)	Models					I_{exp}/I_{th}						
	P_0 (bar)	T_0 (K)	I_b (a.u.)		X_{ico}	X_{cub}	X_f	N_s	T_c	1st (111)	2nd (200)	3rd (220)	4th (311)	5th (400)	6th (331+420)	
6% Ar - He																
Nozzle 11																
12/10/79E	8	233	3	19.1 - 23.5	0.6	0	0.4	3	40	1.05	1.07	1.04	1.01	1	-	1.02
12.5% Ar-He																
Nozzle 11																
2/14/79B	6	255	24	22.54	0.6	0	0.4	3	40	0.96	1.02	1.00	0.97	1	-	0.95
2/21/79B	4	180	64	34.4	0.8	0	0.2	4	50	1.06	0.99	1.00	1.04	1	-	1.05
3/13/79B	4	221	25	18.9 - 21.2	0.6	0	0.4	3	20	1.01	1.00	0.99	1.01	1	-	1.00
3/13/79C	3	205	16	19.7	0.6	0	0.4	3	20	1.00	1.00	1.08	1.04	1	-	0.93
3/19/79A	4	228	135	19.9	0.7	0	0.3	3	40	0.97	0.99	1.01	1.10	1	-	0.98
Nozzle 12																
9/28/79C	8	295	45	23.5	0.7	0	0.3	3	20	1.00	1.00	1.13	1.02	1		0.81

^{a)} See footnotes for Table II.

-33-

Table IV

The Best Fitting Models for Ar Clusters from 25% Ar - He Mixtures^{a)}

Experiment No.	Experimental Conditions			Cluster Size (Å)	Models					I_{exp}/I_{th}						
	P_0 (bar)	T_0 (K)	I_b (a.u.)		X_{ico}	X_{cub}	X_f	N_s	T_c	1st (111)	2nd (200)	3rd (220)	4th (311)	5th (400)	6th (331+420)	
<u>Nozzle 11</u>																
3/1/79B	3	226	2	21.6 - 22.3	0.7	0	0.3	3	20	1.015	0.94	1.00	0.99	1	-	0.95
3/1/79C	2	180	25	24.7	0.8	0	0.2	3	20	1.01	1.03	0.96	0.91	1	-	0.86
3/5/79B	7	210	14	30.5	0.4	0.4	0.2	4	50	1.07	0.98	-	1.00	1	-	0.98
					0.48	0.32	0.2	4	15	1.03	1.02	-	0.90	1	-	0.93
3/6/79C	2	190	16	22.6	0.7	0	0.3	4	20	0.98	1.00	1.02	1.12	1	-	1.09
3/8/79A	6	233	88	27.4	0.64	0.16	0.2	4	20	0.98	0.93	-	1.00	1	-	1
					0.56	0.24	0.2	4	40	1.00	0.85	-	0.95	1	-	0.98
1/24/80C	6.5	291	18	21.4 - 22.9	0.5	0	0.5	3	60	1.03	1.015	1.08	1.02	1	-	1.02
<u>Nozzle 12</u>																
10/9/79A	6	291	36	21.8 - 22.5	0.6	0	0.4	4	40	1.09	0.98	1.02	1.03	1	-	1.02
					0.6	0	0.4	3	20	1.01	0.86	0.97	0.98	1	-	1.02
10/9/79B	7	293	62	26.1	0.6	0	0.4	4	20	1.03	1.00	1.00	1.05	1	-	1.02
<u>Nozzle 13</u>																
2/13/80D	8	292	3	23.5 - 27.4	0.6	0	0.4	4	20	0.98	0.97	0.96	1.00	1	-	-
2/13/80E	9	291	6	25.3 - 29.3	0.6	0	0.4	4	40	0.99	1.02	0.98	1.02	1	-	1.00
					0.6	0	0.4	4	20	1.02	1.01	1.03	1.06	1	-	0.97

^{a)} See footnotes for Table II.

-34-

TABLE V
The Best Fitting Models for Kr Clusters from 6% Kr - He Mixtures a)

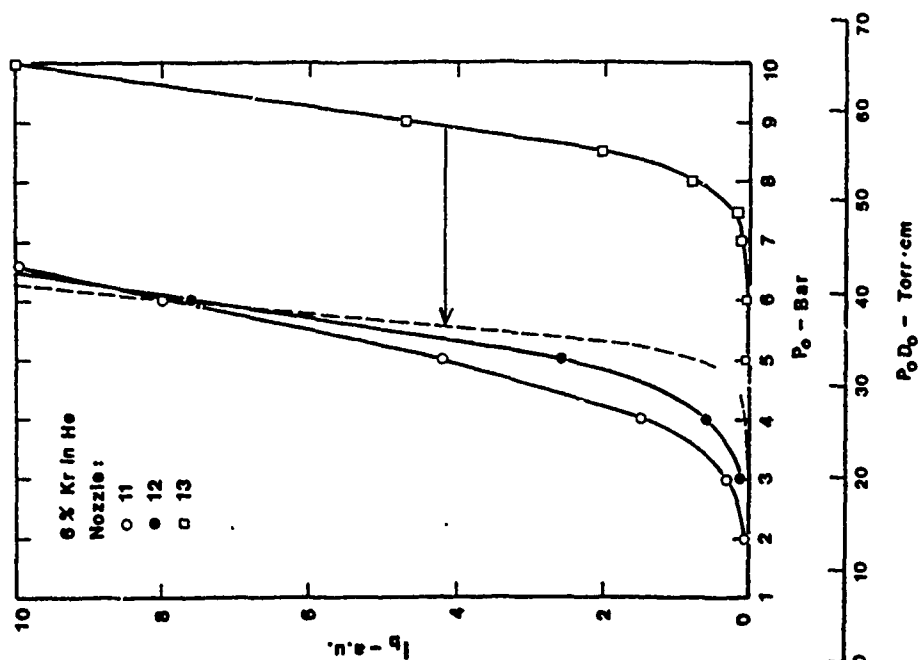
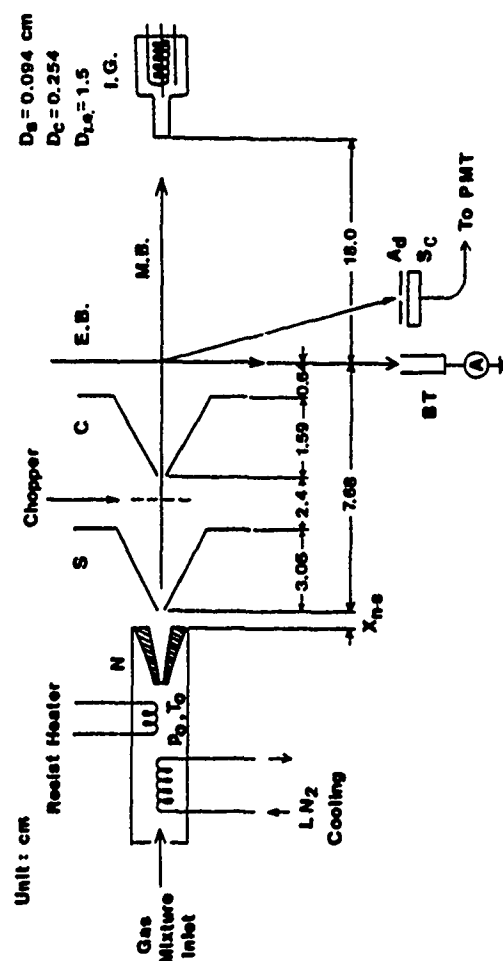
Experiment No.	Experimental Conditions		Cluster Size (Å)	Models				T_c	T_{exp}						
	P_0 (bar)	T_0 (K)	I^b (a.u.)	X_{ico}	X_{cub}	X_f	N_s		1st (111)	2nd (200)	3rd (220)	4th (311)	5th (400)	6th (331+420)	
Nozzle 11	6	292	8	21.2	0.6	0	0.4	3	40	0.96	0.95	1.03	0.97	1	-
4/10/79B	6	292	8	22.6	0.54	0.06	0.4	3	50	0.97	0.96	1.10	1.06	1	-
4/11/79A	4	230	7	19.4	0.7	0	0.3	3	50	0.98	0.93	1.11	1.05	1	-
7/9/79A	7	293	76	18.6	0.5	0	0.5	3	50	0.96	1.01	1.12	1.1	1	-
8/16/79B	4	220	92	20.7	0.6	0	0.4	3	40	0.99	1.02	1.08	1.09	1	-
Nozzle 12	6	293	96	20.5	0.5	0	0.5	3	50	1.02	0.88	1.06	1.07	1	-
10/11/79C	6	293	96	22.5	0.5	0	0.5	3	50	1.02	0.88	1.06	1.07	1	-
Nozzle 13	10	291	11	24.9	0.5	0	0.5	3	20	0.89	0.93	1.00	1.00	1	-
3/28/80C	10	291	11		0.5	0	0.5	3	20	0.89	0.93	1.00	1.00	1	-

a) See footnote for Table II.

TABLE VI
The Best Fitting Models for Xe Clusters from 6% Xe - He Mixtures a)

Experiment No.	Experimental Conditions	Cluster Size (Å)	Models	T_c	1st (111)	2nd (200)	3rd (220)	4th (311)	5th (400)	6th (331+420)							
Nozzle 11	4/17/79A	3	273	5	22.6	0.6	0	0.4	3	60	1.00	1.10	1.10	1	-	0.98	
4/12/79A	4	291	12	22.2	0.6	0	0.4	3	60	0.98	0.99	1.03	1.06	1	-	0.98	
4/17/79B	4	273	15	25.1 ~ 23.8	0.6	0	0.4	3	60	1.04	1.03	1.02	1.06	1	-	1.00	
8/15/79B	3	220	18	24.3	0.6	0	0.4	4	40	1.01	0.99	1.03	1.22	1	-	1.02	
8/16/79A	2.3	218	55	21.9	0.6	0	0.4	3	60	1.08	0.96	1.09	1.14	1	-	0.96	
7/18/79B	5	295	>20	26.3 ~ 27.4	0.6	0	0.4	4	40	1.02	1.02	1.13	1.25	1	-	1.06	
Nozzle 12	12/2/79C	4	291	57	21.4	0.5	0	0.5	3	40	1.02	1.04	1.10	1.14	1	-	1.00
Nozzle 13	2/15/80C	6.25	290	3	25.4 ~ 26.4	0.5	0	0.5	3	40	1.00	0.97	1.09	1.06	1	-	1.00

a) See footnote for Table II.



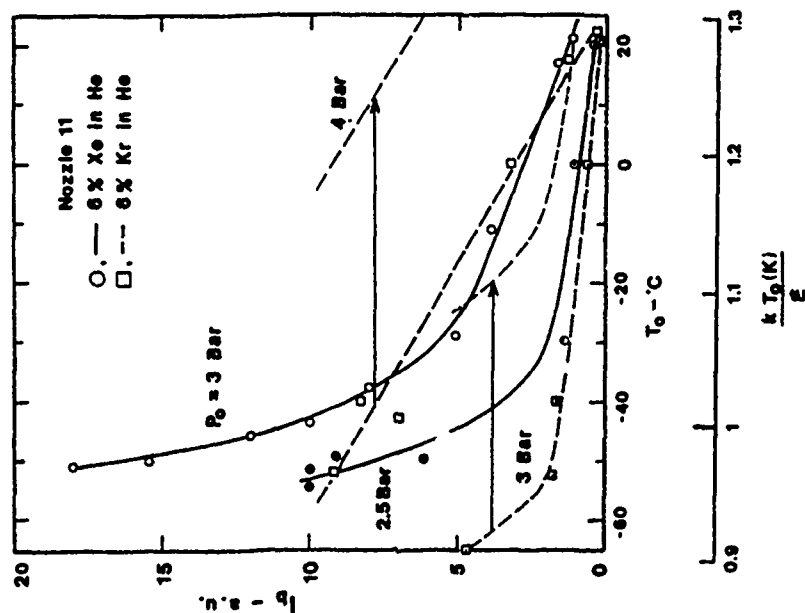


Figure 3

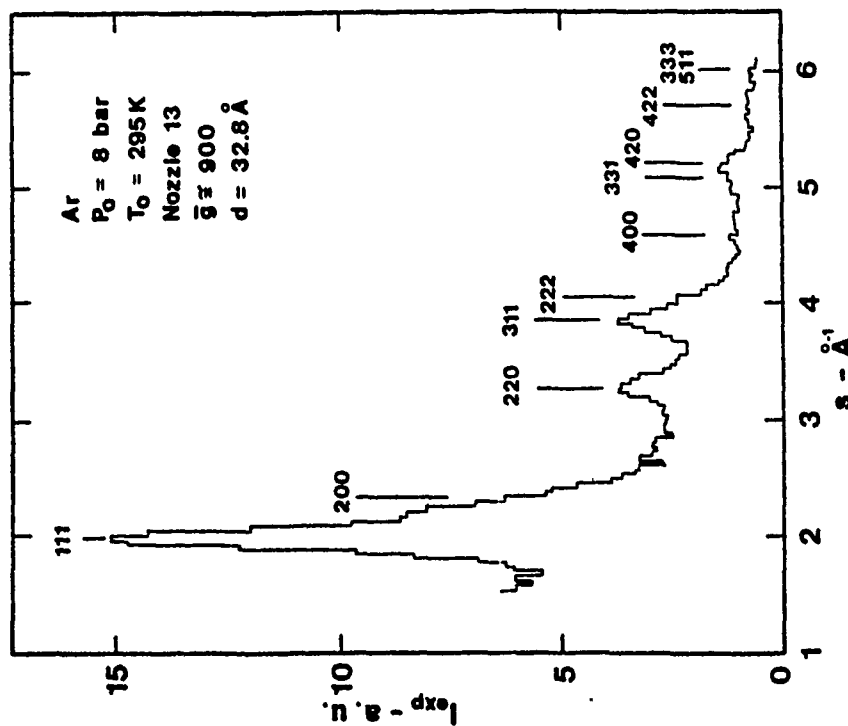


Figure 4

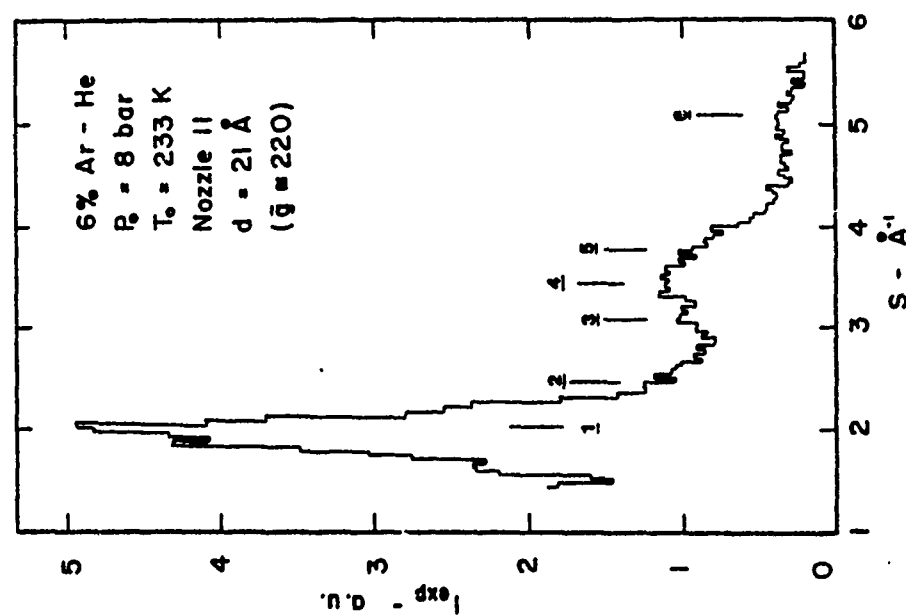


Figure 5

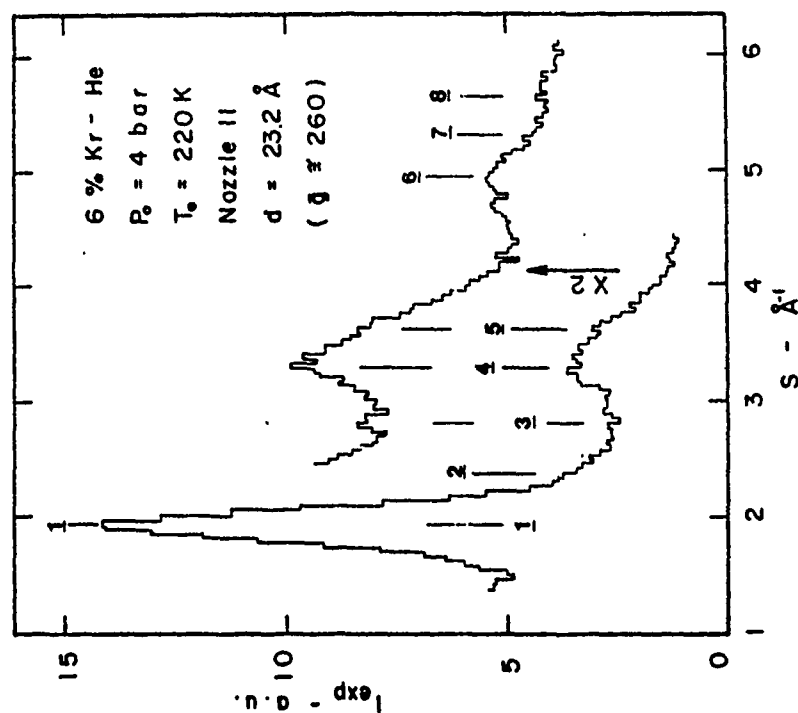


Figure 6

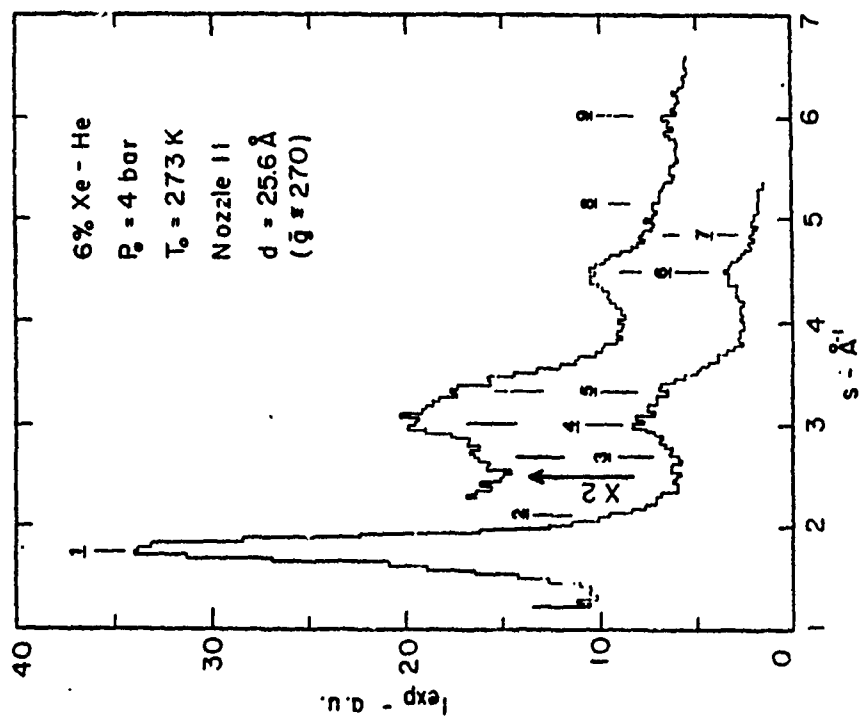


Figure 7

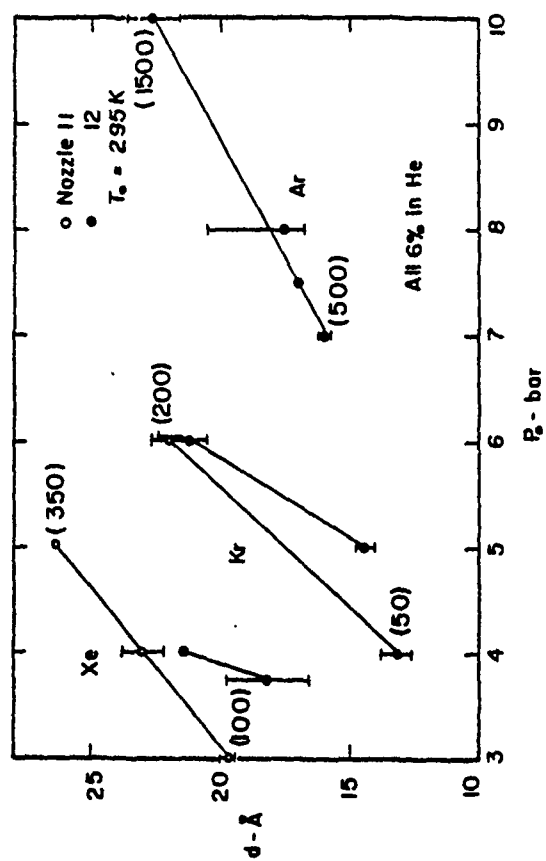
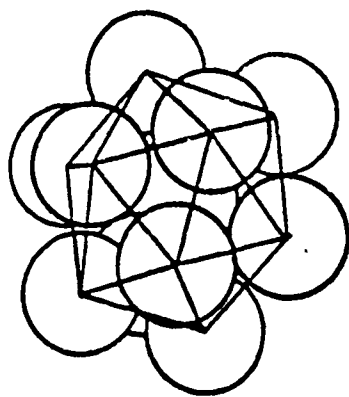
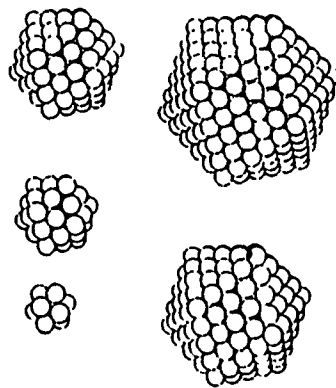


Figure 8

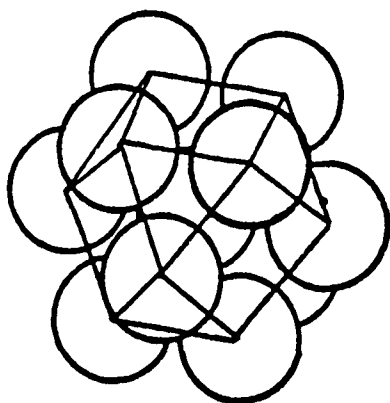


a

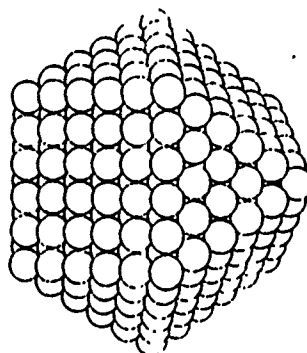


b

Figure 10



a



b

Figure 9

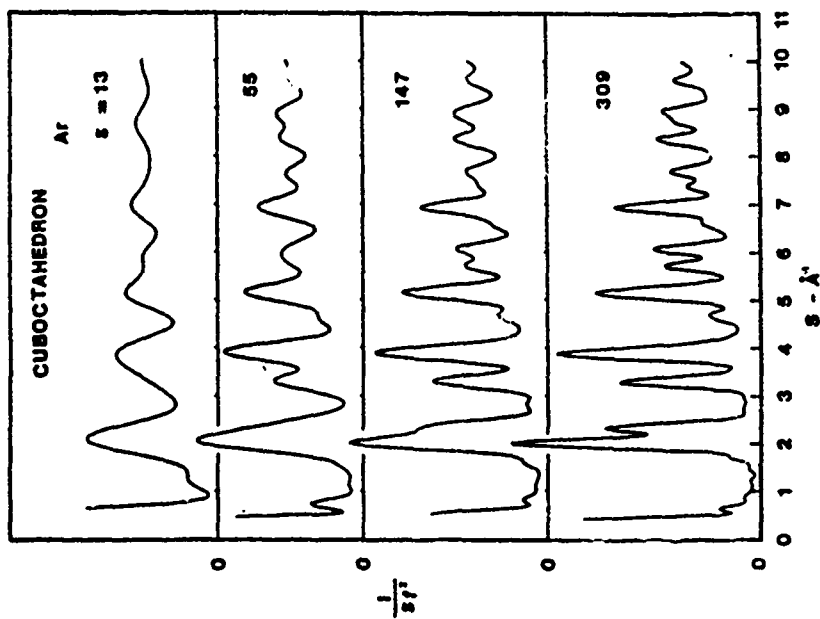


Figure 11

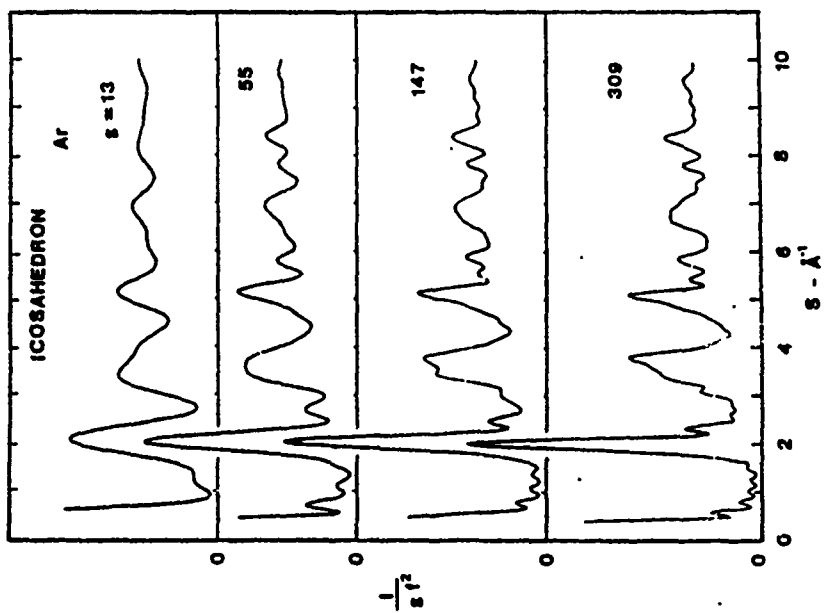


Figure 12

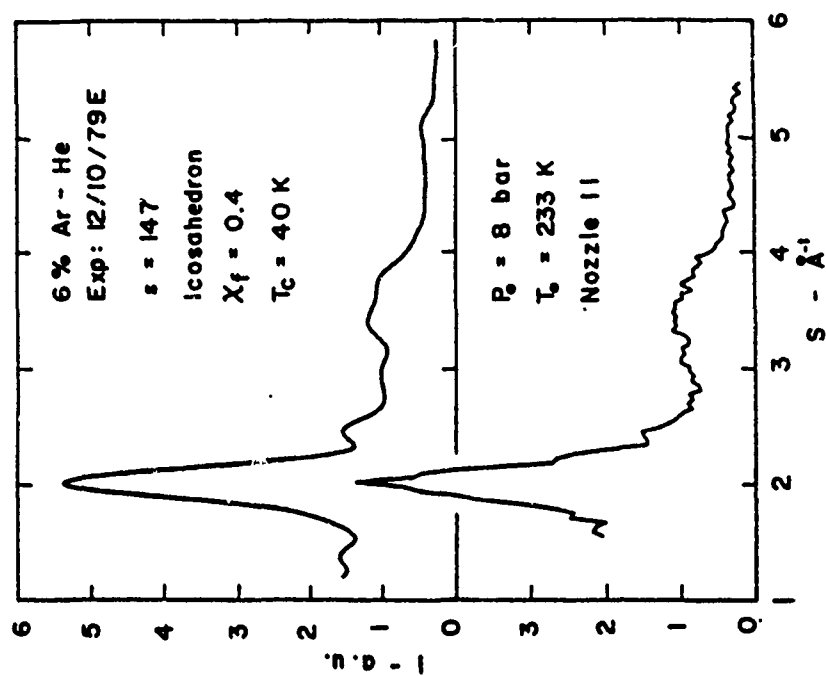


Figure 14

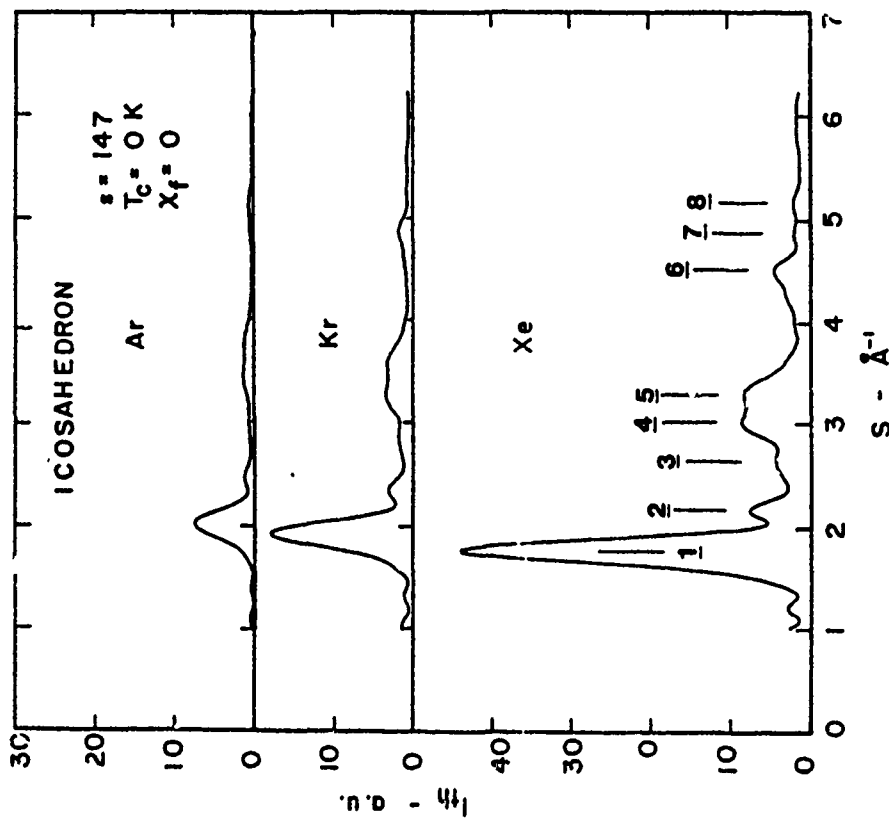


Figure 13

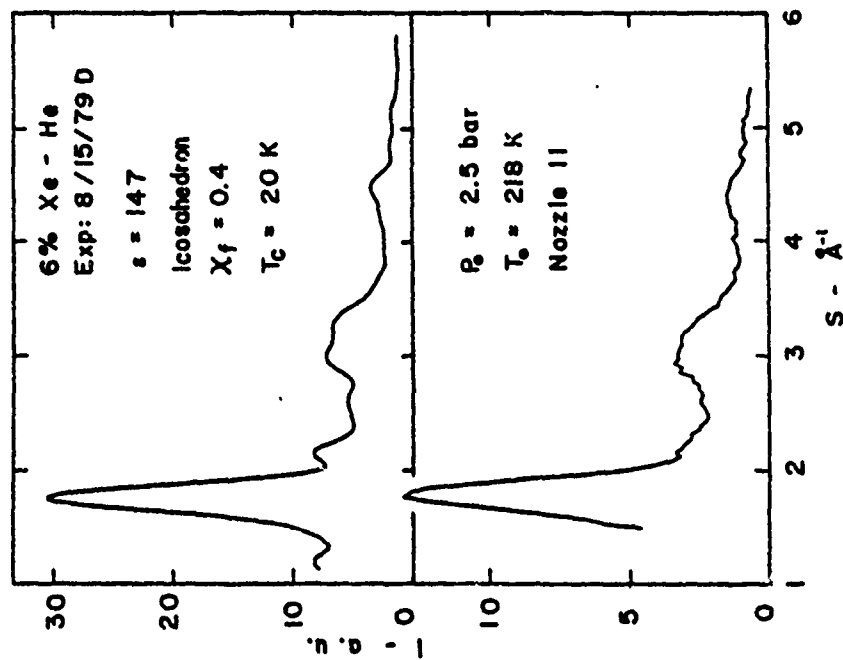


Figure 15

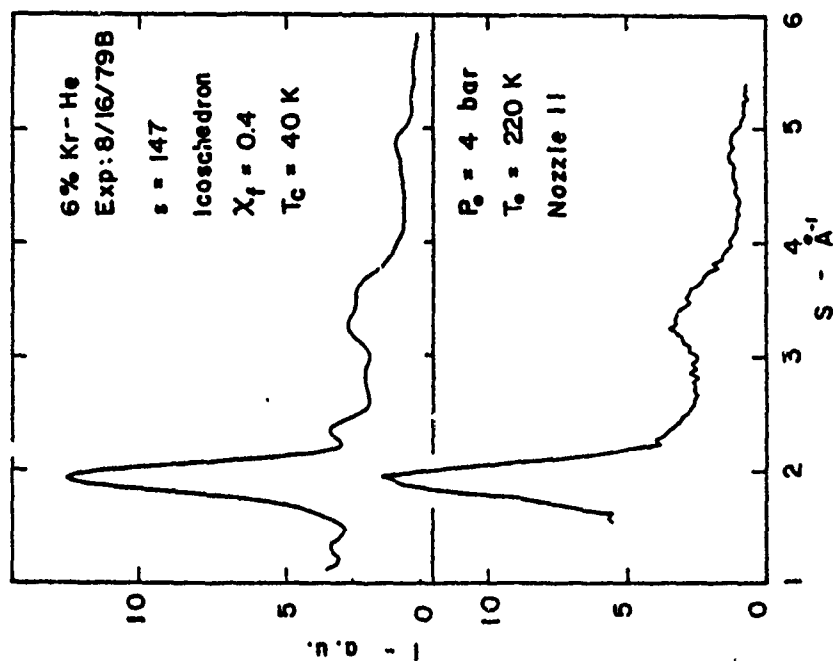


Figure 16